Artificially Engineered Capacitors for Discrete High-Frequency Electronic Circuitry

Tom W. Whittaker, Will G. Whittow, *Senior Member, IEEE*, and John C. Vardaxoglou, *Fellow, IEEE*

Abstract—The concept of the artificially engineered capacitor (AEC) is presented as a 3-D printable 3-D capacitive component for use in discrete RF/microwave electronic circuitry. The intention of the AEC concept is a highly customizable 3-D printable component whose capacitance value is stable over a wider frequency band when compared to commercial alternatives. AECs can be viewed as impedance structures with predominantly capacitive characteristics. Both series and shunt AEC configurations are considered with simulation and measurement data along with equivalent circuit models. The tolerance of the equivalent capacitance over frequency is focused upon in this article. Within the 40% tolerance band from the nominal value an improvement of 26% and 197% frequency band was achieved for the series and shunt variants, respectively, when compared to a commercial alternative. Further simulations show that with finer 3-D printing resolutions, this frequency-stable bandwidth can be further increased. Finally, an example design application of a half-wavelength microstrip resonator is presented in which the AECs' Q factor is measured, and its equivalent circuits are implemented and validated via simulations and measurements.

Index Terms—Artificial dielectrics, capacitors, electromagnetic, electromagnetic devices, microwave components, 3-D printing.

I. INTRODUCTION

ARTIFICIAL materials are becoming more commonplace in antenna and electronic systems. They are intelligently constructed from dielectrics and/or conductors to form new structures with specific and unique electromagnetic characteristics that are not often found in natural materials. Artificial materials are commonly constructed from a periodic array of unit cells; inside each unit cell is an inclusion. For this article, an inclusion can be defined as a metallic mesoscaled particle embedded in a host dielectric material. The dimensions are subwavelength ($<\lambda/10$) and are designed to be operated below their selfresonance. Some examples of inclusions used in 3-D periodic structures are jacks [1], dumbbells [2], and metallic cuboids [3]. It is the characteristics of the inclusions and their interactions with adjacent inclusions that define the overall behavior of the structure. Periodic structures have been applied to many different areas, for example, bandpass metasurface filters [4]–[6], absorbers [7], and antennas [8]–[10]. However, there has been limited progression in developing 3-D periodic structured components for discrete electronic printed circuit board (PCB) applications and systems.

3-D printing technology is becoming a more viable method of manufacture as it offers many advantages over conventional means. In particular, multimaterial printing allows for the opportunity of fully 3-D printed, monolithic, electronic circuits to be manufactured which incorporate multiple different conductors and dielectrics together. The circuit's components and interconnecting transmission lines can all be potentially printed in the same package which allows for greater control over circuit characteristics; for example, component impedance matching and the mitigation of component parasitic effects. The main development of 3-D printed, 3-D circuitry has been aimed at low frequency designs (<100 MHz) that do not consider high frequency issues such as line impedance, impedance mismatches, component parasitic effects, and dielectric or conductor losses [11]–[15]. Attempted 3-D printable circuits and components designed for ultrahigh (0.3–3 GHz) or super-high (3–30 GHz) frequencies are either conventional planar designs that could be made with PCB etching techniques [16]–[19] or 3-D structures whose parasitic elements limit their useful effective frequency range [20]. Attempts at applying artificial materials to microwave structures have mainly been for miniaturization purposes due to their customizable nature. Microstrip transmission line structures [21], [22] and antennas [23] have been investigated with different shapes of metallic inclusions which exhibit the unique properties these materials offer.

Resistors, capacitors, and inductors are the elementary components of any passive high-frequency electronic circuit and are used to design devices which include filters, diplexers, or power dividers. These devices are often realized through discrete lumped element components such as surface mount components. Lumped element components are fundamentally limited by parasitic effects which cause the component's value to vary exponentially until its selfresonant frequency. The parasitic effects originate from the physical construction of the component; for multilayer ceramic capacitors (MLCCs) parasitic series inductance is caused by current paths on the plates and the coupling between them, thus the physical size of the component influences the parasitic inductance [24].

The authors are with the Wolfson School of Mechanical, Electrical and Manufacturing Engineering, Loughborough University, Loughborough LE11 3TU, U.K. (e-mail: t.whittaker@lboro.ac.uk; w.g.whittow@lboro.ac.uk; j.c.vardaxoglou@lboro.ac.uk).
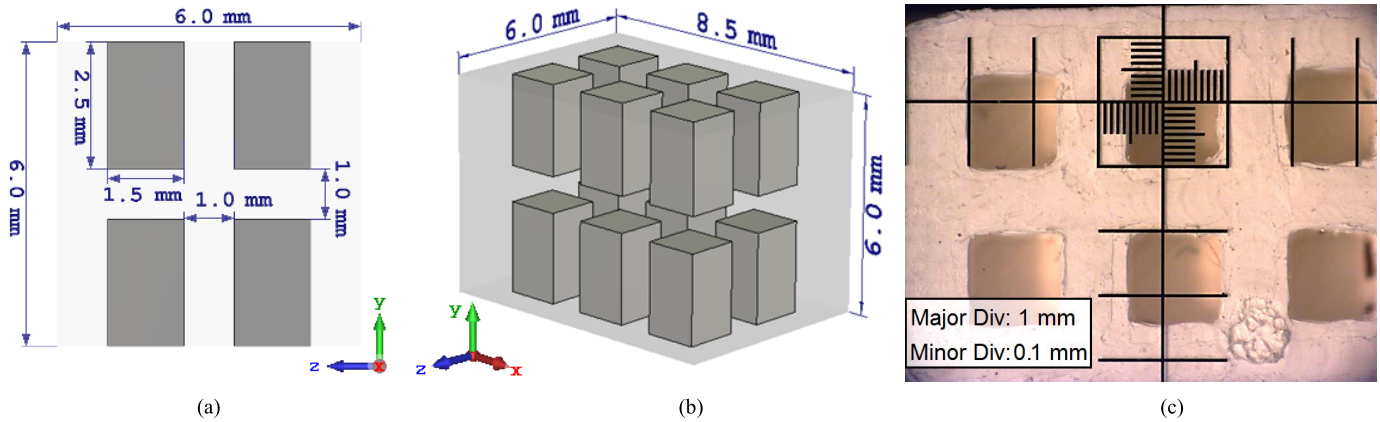
Fig. 1. AEC schematic CAD models and microscope photograph. (a) Side view of AEC CAD model with dimensions. (b) Perspective view of AEC CAD model with dimensions. (c) Closeup microscope photograph of a manufactured AEC with an overlaid glass slide for measuring the dimensions.

The main aim of designing 3-D printable capacitive components is to significantly improve the linearity and stability of the effective capacitance parameter over frequency when compared to current offerings of capacitive devices. Applications that require precise, frequency-stable components, for example, wideband filters, will benefit most from this article.

The proposed artificially engineered capacitor (AEC) designs avoid using an interleaving structure like that seen in MLCCs due to the high parasitic series inductance. The concept is proven with a conventional fused deposition modeling (FDM) 3-D printer as this method is capable of multimaterial printing. This article aims to build the foundations of a palette or library of stock components that can be used in fully 3-D printable, monolithic high-frequency 3-D circuits. The AECs will be tested using conventional PCBs but this work can be transferred to a 3-D printed circuit. This article applies the basic concepts of [3] to a new application of discrete capacitive components for electronic circuits. It is important to note that the AEC is not designed as a replacement of well-established components but as an additional alternative for designers that bring new possibilities to light.

Section II will present the AEC design, describe how they were made, and how they were measured. Section III will display and discuss the measurement data with simulation and equivalent circuit results. Series and shunt configurations will be analyzed and the characteristics compared with commercial MLCCs of equivalent values. Section IV presents potential AEC design variations given fewer manufacturing limitations. Section V shows an example application design for the AEC in a half- wavelength resonator circuit; this example is also used to validate the AEC's equivalent circuit. The resonator is then further used to measure the Q factor of the AEC and MLCC at similar frequencies.

II. DESIGN

The AEC design originates from a periodic artificial dielectric structure comprising of conductive cubic inclusions arranged in a 3-D cubic array. Previous work demonstrated that the permittivity of a bulk dielectric material can be increased and tailored by adding metallic inclusions [3].

This permittivity increase is beneficial for capacitor design. The permittivity can be further controlled by varying the size of the cubic inclusions, the space between them, or changing the host material.

The AECs demonstrated here comprise 12 metallic cuboid inclusions in a $3 \times 2 \times 2$ array with each having dimensions of 1.5 mm $\times$ 1.5 mm $\times$ 2.5 mm and an edge-to-edge spacing between each inclusion of 1 mm, see Fig. 1(a). The overall component size is 6 mm $\times$ 6 mm $\times$ 8.5 mm and each metallic cuboid inclusion is exposed on the top and bottom faces of the AEC to allow direct excitation with an electrical signal, see Fig. 1(b). The 3-D printer used to manufacture the AECs was the Ultimaker 2+ which is only capable of printing the thermoplastic host material. Thus, the host is first printed leaving recesses for the cuboid inclusions. Afterward a conductive epoxy is injected and pressed into the recesses to form the conductive inclusions. The host thermoplastic used was polylactic acid (PLA), which is a widely available and inexpensive material. The material properties were measured at 10 GHz in an X-band waveguide (8–12 GHz) using the Nicolson–Ross–Weir method [25], [26]. The measured relative permittivity was 2.4 and its loss tangent is 0.01. A conductive silver epoxy was used for the conductive inclusions which has a conductivity of 1.43×10^5 S/m [27]. The physical dimensions of the cuboid inclusions were assessed with a microscope to assess the printer's accuracy with the design. Fig. 1(c) shows a close-up photograph of the 3-D printed dielectric host without the metallic inclusions. The overlaid glass slide had major and minor deviations of 1and 0.1 mm, the measured dimensions of the recesses were found to vary within 0.1 mm. The only observable imperfection is with rounded corners of the recesses.

The AECs were designed to be used on a Rogers RO4350B substrate which has a relative permittivity of 3.48, a loss tangent of 0.0037, and a thickness of 0.51 mm. The transmission lines are 1.1 mm wide, which are designed to have a 50-Ω characteristic impedance. The widths of the inclusions were designed to be of similar width to the transmission lines to reduce any impedance mismatch between line and inclusions. From simulating AECs with varying inclusion sizes
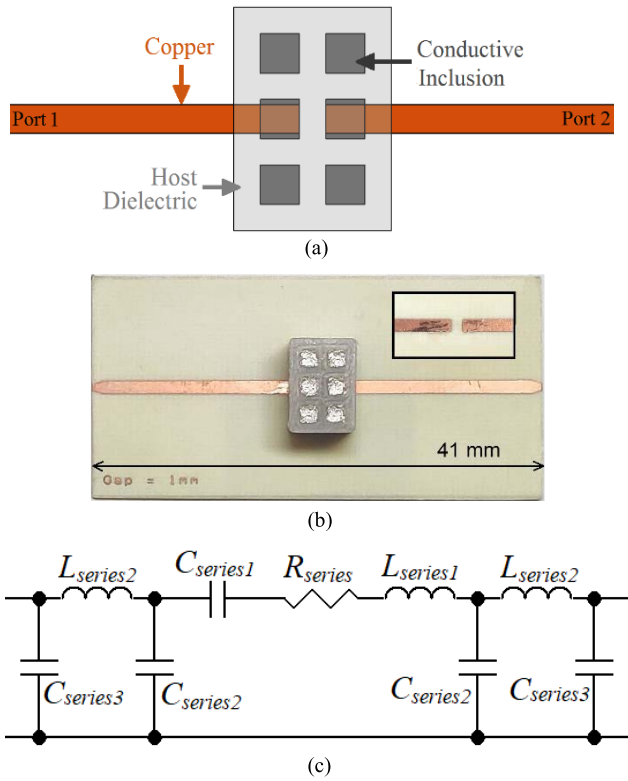
Fig. 2. (a) Series PCB mounted AEC. (b) Photograph of a series PCB mounted AEC with an inset image of the underneath capacitive gap. (c) Equivalent circuit of a series AEC.
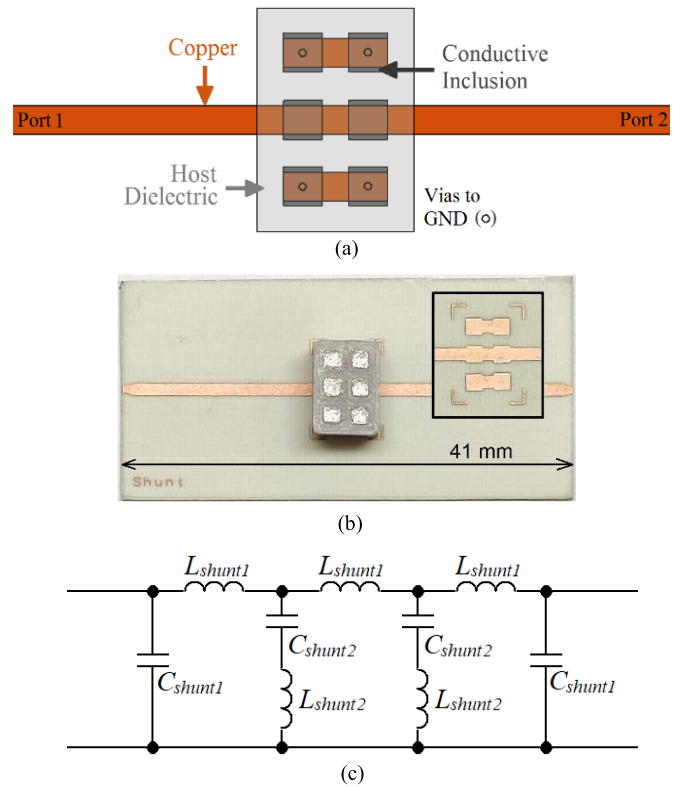

Fig. 3. (a) Shunt PCB mounted AEC. (b) Photograph of a shunt PCB mounted AEC with an inset image of the mounting pads. (c) Equivalent circuit of a shunt AEC.

(using CST), this condition provided the most stable effective capacitance result over frequency. As AECs can be made by the designer, the dimensions and material properties can be tailored to achieve the desired characteristics for the system in mind. In theory, good matching to the component can be obtained for any circuit board system, the only limitation is the resolution of the 3-D printer and the materials available.

A 0.4-mm nozzle was used on the 3-D printer which gave a good compromise between reliable extrusion with no clogging and good printing resolution. Recommended 3-D printing design guidelines also influenced the design of the AEC; "holes" are recommended to be larger than 1 mm in diameter [28] or at least twice the diameter of the nozzle [29] and wall thickness should be at least 1.2 mm [28] or at least twice the diameter of the nozzle [29].

The artificial dielectric has been truncated down to a $3 \times 2 \times 2$ array from an infinite array; this was found to be a good compromise for the overall size of the component between an infinite array and a miniaturized discrete component. The component is designed to be nonresonant as the internal inclusions are much smaller than the wavelength in the circuit. The AECs were measured in both series and shunt configurations. Figs. 2(a) and 3(a) show the layout and mounting of the AEC for series and shunt configurations, respectively, while Figs. 2(b) and 3(b) show the respective fabricated AECs mounted on series and shunt test PCBs. The series PCB has a 1-mm gap in-between two transmission lines where the AEC was placed on top of and conductive

epoxy used to electrically connect the transmission lines to the inclusions. For a higher nominal capacitance value, multiple inclusions can be connected together via the PCB. For the shunt PCB, the AEC was placed on top of the transmission line and the surrounding unconnected inclusions were connected to the ground plane with vias. These vias can be made conventionally; however, in this case the holes were drilled and conductive epoxy was used to make a connection. Four vias were made in total with a diameter of 0.25 mm [see Fig. 3(a)]; this diameter is quite large which helps to reduce the inductance of the vias. Also, the vias are connected in parallel pairs, which further reduce the overall inductance.

Figs. 2(c) and 3(c) show the appropriate equivalent circuits for modeling the series and shunt AECs, respectively. The structure of the equivalent circuits is formed by arranging the reactive circuit elements in accordance with the electromagnetic structure. For the series equivalent circuit, the $C_{series1}$ term represents the capacitive coupling between inclusions, $L_{series1}$ represents the selfinductance of the inclusions and $C_{series2}$ represents the capacitive coupling to ground. The terms $L_{series2}$ and $C_{series3}$ represent the feed inductance to the inclusions and the added capacitive shunt coupling to ground caused by the PLA dielectric on top of the microstrip line. The term R_{series} represents the conductor and dielectric losses of the materials used. For the shunt equivalent circuit, the term C_{shunt2} models the capacitive coupling from the inclusions connected to the transmission line to the inclusions connected to the ground plane and L_{shunt2} models selfinductance of

the inclusions and the vias to the ground plane. The terms L_{shunt1} and C_{shunt1} models the transmission line underneath the component. The circuit values for the series equivalent circuit in Fig. 2(c) are: $C_{series1} = 0.126$ pF, $C_{series2} = 0.4$ pF, $C_{series3} = 0.12$ pF, $L_{series1} = 1$ nH, $L_{series2} = 0.29$ nH, and $R_{series} = 2$ Ω. The circuit values for the shunt equivalent circuit in Fig. 3(c) are: $L_{shunt1} = 0.29$ nH, $L_{shunt2} = 0.25$ nH, $C_{shunt2} = 0.45$ pF, and $C_{shunt1} = 0.12$ pF. The terms $C_{series1}$ and C_{shunt2} dominate the components' characteristics at dc and the terms $L_{series1}$ and L_{shunt2} contribute the most to the selfresonant frequency of the AECs, thus estimated values can be calculated from the selfresonance and the nominal capacitance. The terms $L_{series2}, C_{series3}, L_{shunt1}$, and C_{shunt1} represent the small transmission line segment within the component that is covered by dielectric. Design equations presented by Barbuto *et al.* [30] can be used to calculate the effective permittivity of microstrip line section with the dielectric cover. The effective permittivity can then be used in conjunction with the conventional microstrip line design equations to calculate the characteristic impedance Z_0 and phase velocity v_p [31]. Using these two identities, the inductance and capacitance values per unit length can be calculated. The terms $L_{series2}, C_{series3}, L_{shunt1}$, and C_{shunt1} can be calculated using the following equations, where ε_{reff} is the effective permittivity of the microstrip line with the dielectric overlay:

$$v_p = \frac{3 \times 10^8}{\sqrt{\varepsilon_{reff}}} = \frac{1}{\sqrt{LC}} \tag{1}$$

$$Z_0 = \sqrt{L/C}. \tag{2}$$

After that, the remaining L and C terms in the equivalent circuit are then computed using an iterative curve-fitting tool which evaluates the measured and simulation data (from CST) to arrive at appropriate values. These equivalent circuits were only designed to be accurate below the selfresonant frequency and are not accurate after selfresonance.

A Wiltron 3680K test fixture and an Anritsu MS46522B vector network analyser (VNA) was used to measure the AECs; (3)–(5) were then used to calculate the impedance of series and shunt component, respectively, and their respective effective capacitance. Derivations of (3) and (4) can be found in the appendix. Equation (5) can be rearranged to calculate the effective capacitance from impedance [31]

$$Z_{DUT} = 2Z_0 \frac{S_{11}}{S_{21}} \tag{3}$$

$$Z_{DUT} = -0.5Z_0 \frac{S_{21}}{S_{11}} \tag{4}$$

$$Z_{DUT} = \frac{1}{j2\pi f C_{eff}}. \tag{5}$$

Here Z_0 is the characteristic impedance of the line (in this case 50 Ω), S_{11} and S_{21} are the measured reflection and transmission coefficients, respectively. Z_{DUT} is the impedance of the component or device under test (DUT), f is the excitation frequency, and C_{eff} is the effective capacitance value.

For a comparison, the AEC data were plotted alongside measured equivalently valued 0603 (IN) (1.6 mm × 0.8 mm × 0.8 mm) MLCCs. MLCCs valued at 0.1 and 1 pF were

TABLE I
AEC ESTIMATED COST BREAKDOWN

Material	PLA	Conductive Silver Epoxy
Cost of bulk material	£28.32 [34]	£70.66 [35]
Mass of bulk material (g)	1000	21
Average material mass measured (mg)	272.8	124.6
Material Cost in each AEC	£0.008	£0.419

measured in a series-thru and shunt-thru fixtures, respectively. Both MLCCs were manufactured by AVX and are from their multilayer organic capacitors (MLO) line of ceramic capacitors. To ensure the MLCC measurements conducted in this article are valid, the measurements were compared against the manufacturer's own measurement data [32]. Fig. 4 shows the close agreement of the authors' measurements and the manufacturer's measurements. Thus, the authors are confident of the accuracy of the measurement and data extraction process. The effective capacitance curve is characteristic of a chip capacitor; the nominal value is close to the stated value but as the operating frequency increases so does the effective capacitance value which is a consequence of the internal parasitic inductance [24]. The selfresonant frequencies are close between the authors' and the manufacturer's measurements. However, as MLCCs are not designed to be operated at selfresonance this value can have a wide variance in practice. Furthermore, the choice of substrate can also influence selfresonance.

Owing to 3-D printing restrictions, the AEC is larger than the MLCC with an outer dimension of 6 mm × 6 mm × 8.5 mm compared to 1.6 mm × 0.8 mm × 0.8 mm for the MLCC. This means the MLCC has a higher capacitance to volume ratio than the AEC. The MLCC achieves this with its internal interleaved structure which exhibits a high capacitance advantage; the drawback with this structure is the high parasitic inductance that is introduced. With higher permittivity materials and increased 3-D printing resolutions, the AEC capacitance to volume ratio could be improved, resulting in a wideband component that is of comparable size.

For a comparison of cost, at the time of writing the current unit cost of individually purchased MLCCs is £0.611 and £0.507 for the 0.1- and 1-pF capacitors, respectively [33]. The material cost of the AECs can be calculated by the cost of a PLA filament spool and the silver epoxy vials multiplied by the respective fraction of materials used. Table I shows the breakdown of the cost. The mass of five 3-D printed AECs with no conductor was measured and an average was taken to obtain the average dielectric material mass. The AECs were then filled with the conductive epoxy and re-measured. The difference in mass corresponds to the amount of epoxy used. An average of this value was then taken as shown in Table I.

This total material cost of the AEC is £0.427 which is less expensive than a single MLCC. It is worth noting that the material cost calculated for the AEC is for small-scale production and not mass manufacture as production scale would affect the end price. Furthermore, AEC manufacture
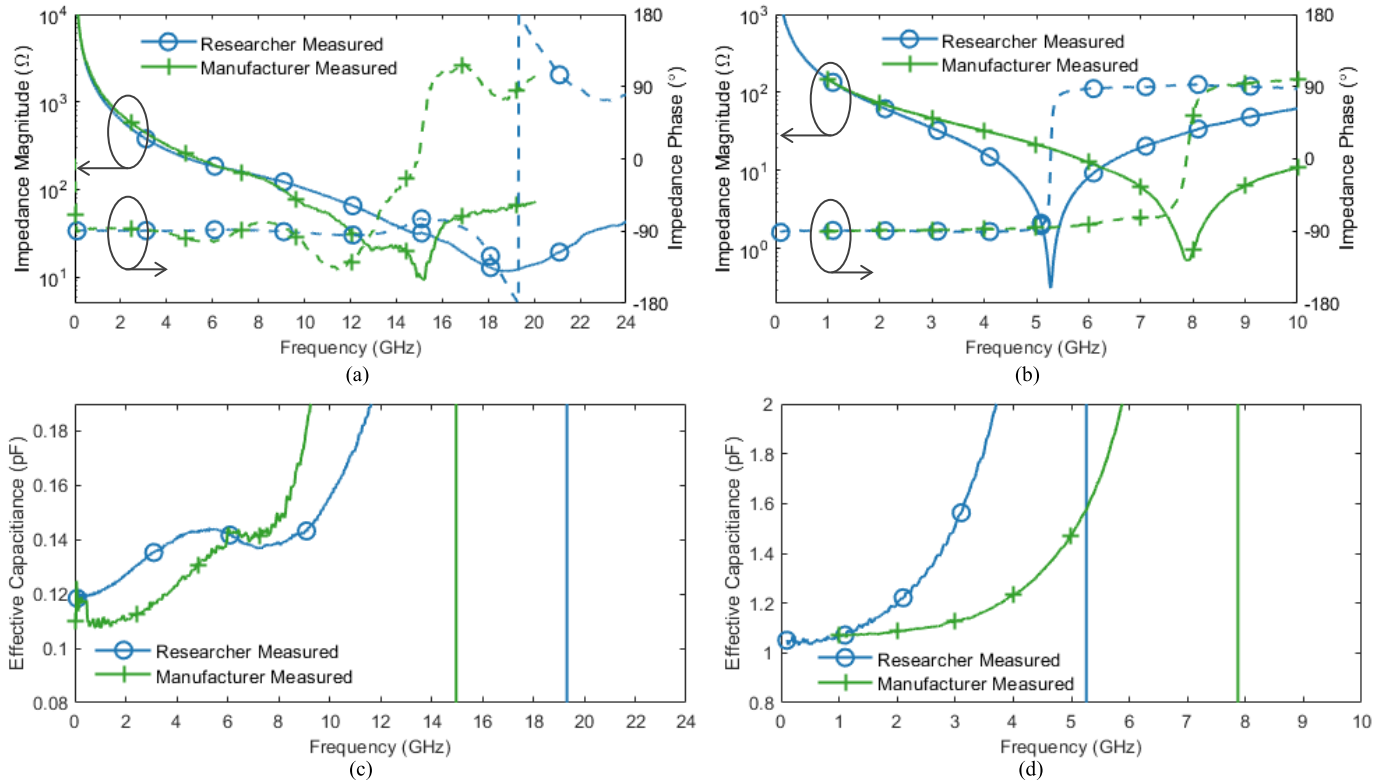
Fig. 4. Comparison of researcher and manufacturer measured series and shunt mounted MLCCs. (a) Comparison of the impedance phase and magnitude of the series 0.1-pF capacitors. (b) Comparison of the impedance phase and magnitude of the shunt 1-pF capacitors. (c) Effective capacitance comparison plot of the series 0.1-pF capacitors. (d) Effective capacitance comparison plot of the shunt 1-pF capacitors.

has some significant advantages over MLCC production. First, the infrastructure cost for MLCCs is higher as AECs can be made entirely with a dual extrusion 3-D printer, thermoplastics, and room temperature curable liquid conductors. MLCCs require a multistage process, which includes screen printing, cutting, high temperature sintering, and termination plating. Last, 3-D printers are more flexible and can easily adapt to changes rather than having to buy new "tooling" if changes to the component design are made.

III. MEASUREMENT RESULTS

A. Series Configuration

The series AEC simulation and measurements are in good agreement as shown in Fig. 5(a)–(c), though there is some slight deviation near selfresonance. The synthesized equivalent circuit, proposed in Fig. 2(c), also shows good agreement with the measured results up to selfresonance. The measured results for the series AEC and equivalent MLCC are shown in Table II.

The selfresonance of the measured AEC can be seen to have a value of 16.3 GHz which can be identified by impedance phase intersecting 0°. While at selfresonance the AEC's impedance is greater than the equivalent MLCC; the majority of losses at this point are from radiation into free space as found from analyzing simulation results. This is not an issue, however, as the component is designed to operate below the selfresonant frequency. The losses can also be viewed in Fig. 5(b) as this causes the phase change

TABLE II
AEC AND MLCC MEASURED SERIES PERFORMANCE COMPARISON

Property	MLCC	AEC
Nominal capacitance	0.118 pF	0.122 pF
±20 % tolerance bandwidth	Up to 5.4 GHz	Up to 3.2 GHz
±40 % tolerance bandwidth	Up to 10.8 GHz	Up to 13.6 GHz
Self-resonant frequency	19.0 GHz	16.3 GHz
Component size	$1.6 \times 0.8 \times 0.8$ mm^3	$6 \times 6 \times 8.5$ mm^3

across 0° to not be as sharp as the MLCC. MLCCs also suffer with radiation losses, however, due to their smaller size this only becomes significant at much higher frequencies. Reducing AECs feature sizes would also reduce the radiation losses before selfresonance.

As can be seen in the effective capacitance plot in Fig. 5(c) and Table II the effective capacitance value is more frequency-stable in the 40% tolerance band which shows a 26% improvement over the MLCC. Even though the MLCC used for comparison is much smaller in size, the AEC's characteristics and performance are comparable. As previously stated in Section II, the main limitation with 3-D printed AECs is the achievable reliable resolution of current FDM 3-D printers.

B. Shunt Configuration

The shunt AEC's simulation and measurement results are in good agreement with slight deviation near selfresonance,
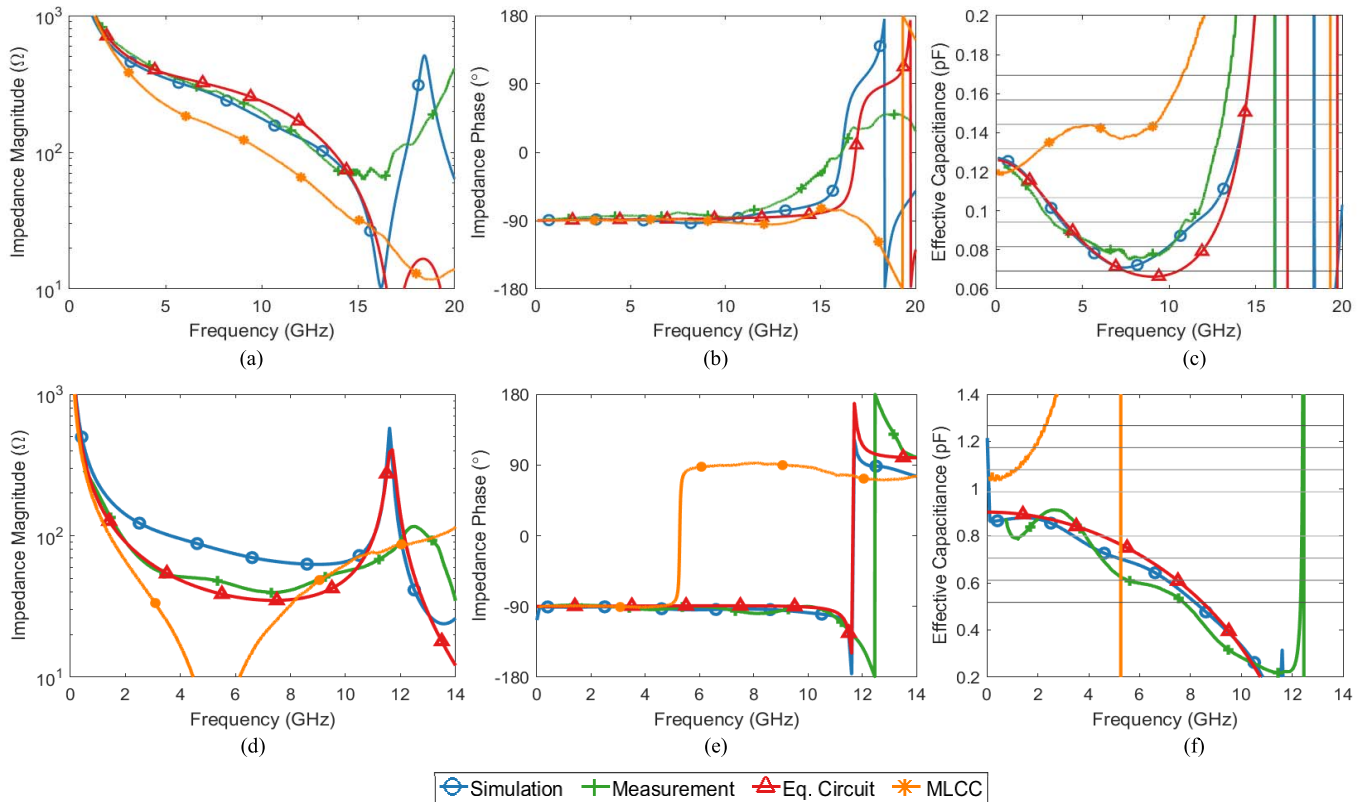
Fig. 5. Measurement, simulation, and equivalent circuit analysis plots, compared with a measured commercial MLCC, of both series and shunt AECs. (a) Series AEC impedance magnitude plot. (b) Series AEC impedance phase plot. (c) Series AEC effective capacitance plot with overlaid tolerance lines over frequency at ±10%, ±20%, ±30%, and ±40% from the nominal value. (d) Shunt AEC impedance magnitude plot. (e) Shunt AEC impedance phase plot. (f) Shunt AEC effective capacitance plot with overlaid tolerance lines over frequency at ±10%, ±20%, ±30%, and ±40% from the nominal value.

TABLE III
AEC AND MLCC MEASURED SHUNT PERFORMANCE COMPARISON

Property	MLCC	AEC
Nominal capacitance	1.0 pF	0.9 pF
±20 % tolerance bandwidth	Up to 2.0 GHz	Up to 5.0 GHz
±40 % tolerance bandwidth	Up to 2.7 GHz	Up to 8.1 GHz
Self-resonant frequency	5.3 GHz	12.5 GHz
Component size	$1.6 \times 0.8 \times 0.8$ mm^3	$6 \times 6 \times 8.5$ mm^3

see Fig. 5(d)–(f). The equivalent circuit proposed in Fig. 3(c) also shows good agreement with the measured results. The measured results for the shunt AEC and equivalent MLCC are shown in Table III.

The selfresonant frequency of the shunt AEC has dramatically increased compared to the MLCC, from 5.3 to 12.5 GHz. This means that the AEC exhibits capacitive properties over a wider frequency range. When comparing results in Fig. 5(f) and Table III the AEC's effective capacitance remains in the 20% and 40% tolerance bands over a wider frequency; a 150% increase in the 20% tolerance band and a 197% increase in the 40% tolerance band have been achieved. The AEC's effective capacitance value is more uniform over a wider frequency range when compared to the MLCC even though the overall component footprint is larger. This conveys great

benefits, especially in wideband applications, as frequency-stable components make such systems much easier to design and implement. The phase change in Fig. 5(e) for the shunt AEC is also quite sharp which indicates low losses in the component especially near selfresonance.

IV. DESIGN VARIATIONS

Currently the achievable capacitance of the AECs shown is quite small at under 1 pF. This is largely due to the limited availability of high permittivity 3-D printable filaments and relatively low 3-D printer resolution, compared to MLCC, LTCC, and PCB manufacturing techniques. However, with emerging technologies, structures in future can be printed at micron scales and with high permittivity materials, such as cold sintered ceramics [36]–[38]. In this section, Figs. 6–8 show graphs of capacitance over frequency for design variations assuming no manufacturing limits. These variations include larger inclusions, reduced inclusion spacing, scaling the AEC down in size and changing the AEC's host permittivity. These figures demonstrate how the nominal capacitance can be increased and how the capacitance variation over frequency can be reduced.

A. Inclusion Spacing and Size

A potential way to increase the nominal capacitance is to either increase the surface area of the inclusions or to reduce their spacing. Fig. 6(a) and (b) shows the simulated series
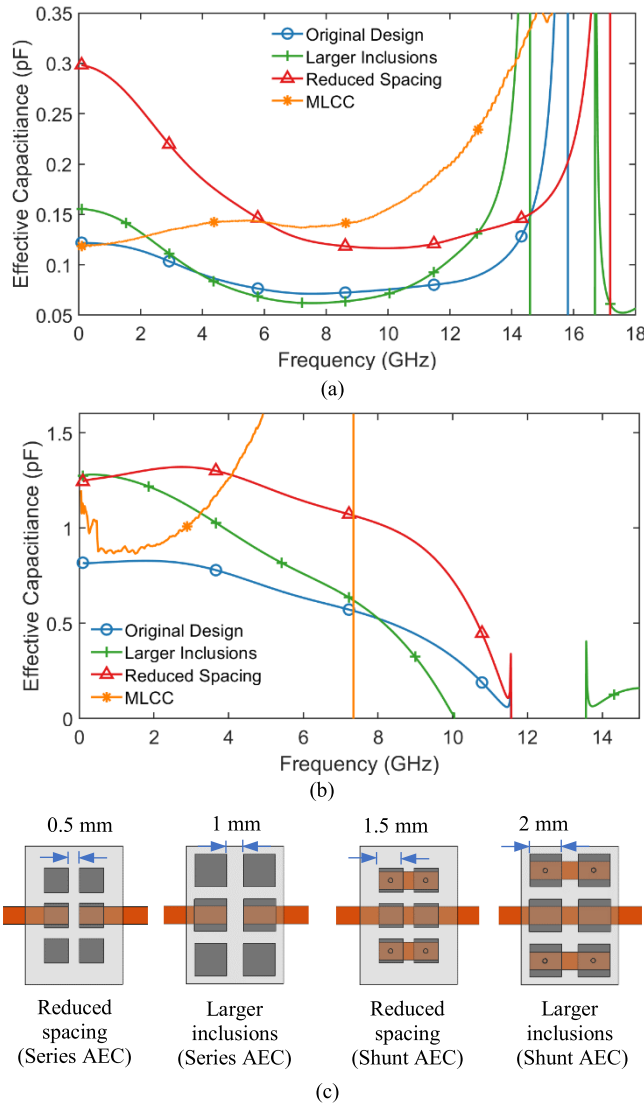
Fig. 6. Simulated effective capacitance plot comparing the original AEC, an equivalent valued measured MLCC design and an AEC with 0.5 mm larger inclusions and an AEC with inclusion spacing reduced by 0.5 mm. (a) Series configuration. (b) Shunt configuration. (c) Visualization of the changes.
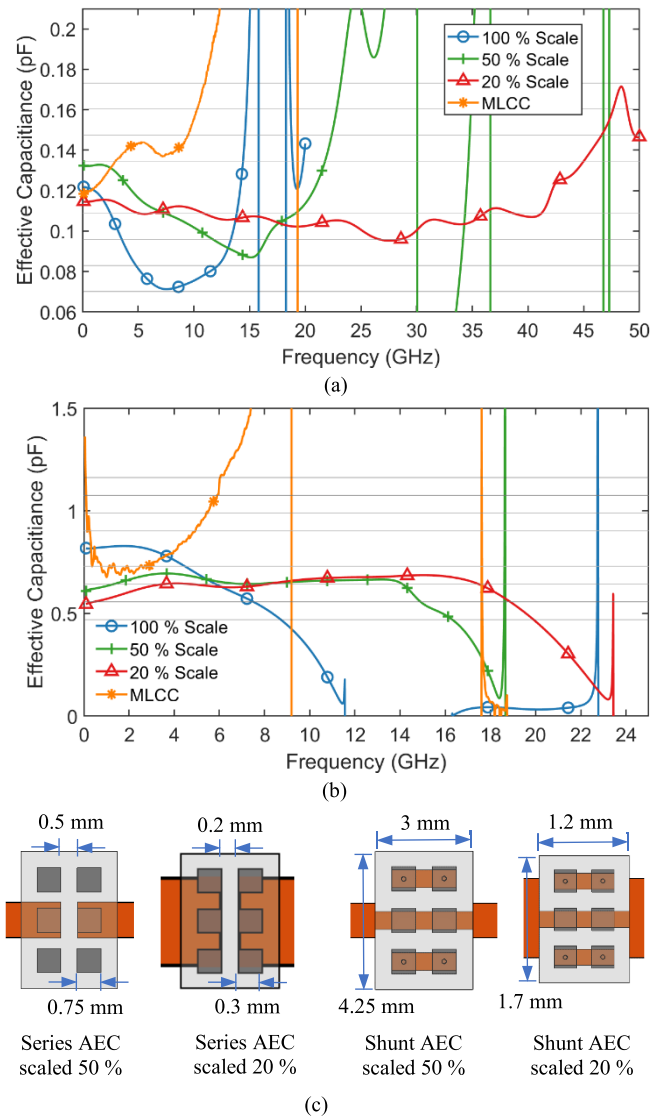

Fig. 7. Simulated effective capacitance plot of the AECs when scaled at 100%, 50%, and 20% and an equivalently valued measured MLCC. The host permittivity is changed to maintain a similar nominal capacitance value. (a) Series configuration. (b) Shunt configuration. (c) Visualization of the scaled AECs.

and shunt-effective capacitance curves, respectively, for the original AEC compared with two design variations. The first variation increases the inclusions in all directions by 0.5 mm whilst the second variation reduces the spacing in-between inclusion by 0.5 mm while retaining the original inclusion size. Changes are depicted in Fig. 6(c).

For the series AEC, the nominal capacitance value has increased in both variations, however, the capacitance stability over frequency has reduced which is due to the increased capacitive coupling to ground. For the shunt case, both variations resulted in the same increase to the nominal capacitance. However, with reduced inclusion spacing the capacitance value is more stable over frequency. This is most likely due to the smaller elements having lower parasitic effects.

B. Miniaturization

Another possible design variation is to scale the dimensions. By shrinking the design, radiation losses at lower frequencies would be reduced, the selfresonant frequency would be increased, and the AEC would also be more comparable in size to current commercial offerings. When scaled to 50% the overall dimensions would be 3 mm × 3 mm × 4.25 mm and each inclusion would have a size of 1.25 mm × 0.75 mm × 0.75 mm. When scaled to 20% the overall component dimensions would be 1.2 mm × 1.2 mm × 1.7 mm and each inclusion would have a size of 0.3 mm × 0.3 mm × 0.5 mm, this overall size is comparable to the 0603 MLCCs used for comparison in this article. Shrinking the AEC would reduce the inclusion spacing thus increasing capacitance, however, the reduction in inclusion surface area overall decreases capacitance. To maintain a similar nominal capacitance value the permittivity of the host must be increased or more inclusions connected to the transmission lines.

For 50% scaled series and shunt AECs, the host dielectric relative permittivity was increased to 4.5. However, for
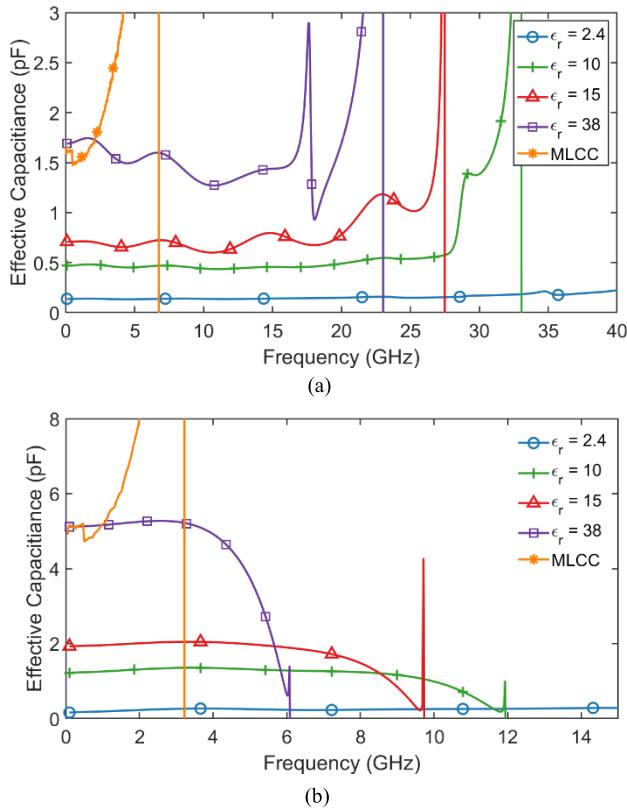
Fig. 8. Simulated effective capacitance plot of the AECs with different host dielectrics compared to a measured MLCC. The AEC host relative permittivities used are 2.4, 10, 15, and 38. The series and shunt AECs scaled to 20% and 50% of their original dimensions, respectively. (a) Series configuration. (b) Shunt configuration.

the 20% scaled AECs the component width was close to the width of the transmission line. This allowed two more inclusions to be connected to either side of the capacitive gap for the series AEC. The host relative permittivity was kept at 2.4 to obtain a nominal capacitance close to 0.12 pF.

For a shunt AEC scaled to 20%, the host's relative permittivity was increased to 10 to overcome the capacitance loss due to reduced inclusion surface area. In addition, the transmission lines running underneath the component were also reduced to 0.3 mm in width to avoid the vias underneath the outer inclusions short-circuiting the transmission line. Note, 3-D printable filaments of relative permittivity of 4.5 and 10 are currently available from Premix (PREPERM ABS450 and ABS1000) as a ceramic loaded acrylonitrile butadiene styrene (ABS)-based material [39]. Fig. 7(a) and (b) shows the comparison of the simulated series and shunt-effective capacitance curves, respectively, for an AEC at 100%, 50%, and 20% scaling factors. As the AEC is reduced in size, the selfresonance frequency is increased, and the effective capacitance is more stable over frequency. The 40% tolerance band for the series configuration is increased to 23.2 GHz for a 50% scaled AEC and >50 GHz for a 20% scaled AEC. While the 40% tolerance band for the shunt configuration is increased to 16.1 GHz for a 50% scaled AEC and 19.9 GHz for a 20% scaled AEC.

AECs benefit greatly from miniaturization though an increase to host permittivity or more connections to inclusions is needed to overcome the reduced inclusion surface area.

C. Alternative Host Dielectrics

Varying the host permittivity of the AECs is a simple way of changing the nominal capacitance. However, when using higher permittivity dielectrics, care needs to be taken to ensure that the inclusions are not resonant within the desired operating frequency band which can cause increased losses and unwanted variations in the capacitance value over certain frequencies. For the simulations, the relative permittivity of the host material for the AECs was set to 2.4, 10, 15, and 38 to give a wide range of varying nominal capacitances. The series AEC was scaled to 20% and the shunt AEC was scaled to 50% to make the size similar to that of the MLCC for a fairer comparison of performance.

Fig. 8(a) and (b) shows the series and shunt capacitance values, respectively, over frequency. As shown, increases in host permittivity increase the nominal value while also decreasing the selfresonance of the component. When the relative permittivity is 38 there is a large amount of coupling to ground; this is beneficial to the shunt AEC but not to the series AEC. Thus, to reduce this coupling, selectively printing high permittivity materials in the center of the component may be a good option for reducing the fields at the edges of the microstrip line. The largest nominal capacitances achieved in Fig. 8 are 1.7 pF for the series AEC and 5.1 pF for the shunt AEC.

V. AEC RESONATOR AND Q-FACTOR MEASUREMENTS

This section demonstrates the AEC in a typical half wavelength microstrip resonator. The resonator consists of a resonant half wavelength transmission line capacitively coupled at each end by either a capacitive microstrip gap or with an AEC. The series equivalent circuit derived in Section II was also validated and compared here to simulation and measurement results. The equivalent circuits were formed from transmission (ABCD) matrices which allow parts of the circuit to be modeled separately. The PCB substrates used for both resonators were the same used in Section III; Rogers RO4350B ($\varepsilon_r = 3.48$, $\tan(\delta) = 0.0037$, thickness = 0.51 mm). The resonator is also used to take Q factor measurements for the AEC and the 0.1-pF MLCCs for comparison.

A. Microstrip Gap Resonator Equivalent Circuit

For the gap resonator, the resonating element was designed to be 10 mm in length with a capacitive gap length of 0.2 mm either side of the resonator as shown in Fig. 9. The widths of the leading transmission lines and resonator were 1.1 mm giving a characteristic impedance of 50 Ω, while the leading transmission lines have a length of 20 mm. A photograph of the resonator can be seen in Fig. 9(a). The equivalent circuit can be split into five sections; three transmission line sections and two capacitive sections, see Fig. 9(c). The transmission line sections can be modeled by the following equation [31]:

$$ABCD = \begin{bmatrix} \cos(\beta l) & jZ_0\sin(\beta l) \\ j/Z_0\sin(\beta l) & \cos(\beta l) \end{bmatrix}. \quad (6)$$

The terms β, Z_0, and l represent the propagation constant, characteristic impedance, and the length of the line,
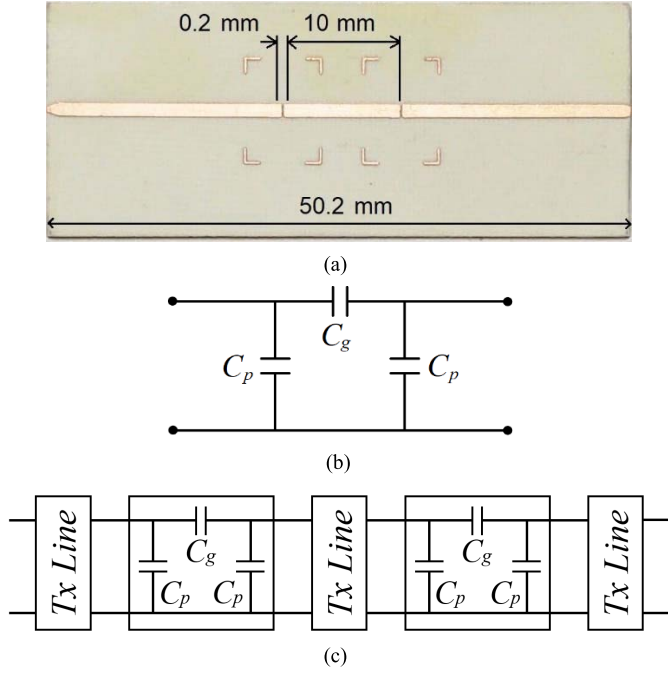
(a)

(b)

(c)

Fig. 9. (a) Photograph of the microstrip gap resonator. (b) Equivalent circuit for a capacitive microstrip gap. (c) Equivalent *ABCD* circuit model of the microstrip gap resonator.
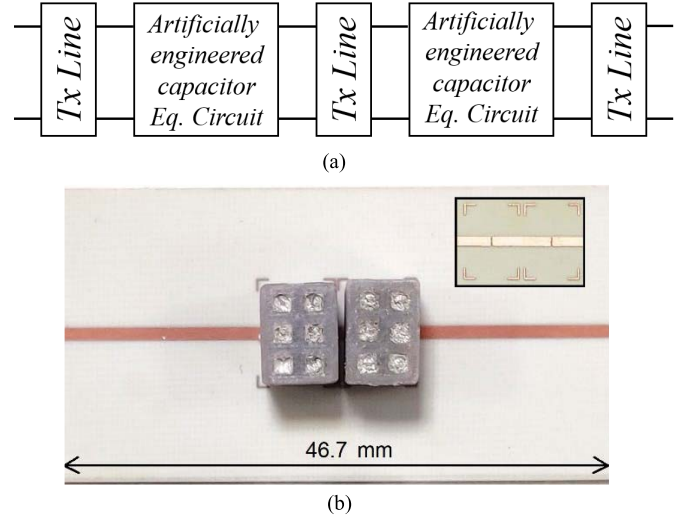

(a)

(b)

Fig. 10. (a) Equivalent *ABCD* circuit model of the microstrip AEC resonator. (b) Photograph of the AEC resonator with inset show resonating element.

respectively. The propagation constant and characteristic impedance of a microstrip transmission line are well known and can be found in many fundamental microwave engineering textbooks [31].

The capacitive microstrip gaps can be modeled by a π network shown in Fig. 9(b), where the central series capacitance C_g models the capacitive coupling across the gap and the two shunt capacitances C_p model the stray capacitive coupling from each transmission line end to the ground plane. The following equations are used to calculate the gap and parallel capacitances (C_g and C_p), respectively [40]:

$$C_g = 0.5C_o - 0.25C_e \tag{7}$$
$$C_p = 0.5C_e. \tag{8}$$

The terms C_e and C_o relate to the gap and parallel capacitances by [40]

$$\frac{C_O}{W}(\text{pF/m}) = \left(\frac{\varepsilon_r}{9.6}\right)^{0.8} \left(\frac{s}{W}\right)^{m_o} e^{k_o} \tag{9}$$

$$\frac{C_e}{W}(\text{pF/m}) = 12\left(\frac{\varepsilon_r}{9.6}\right)^{0.9} \left(\frac{s}{W}\right)^{m_e} e^{k_e} \tag{10}$$

where

$$m_o = \frac{W}{h}\left[0.619\ln\left(\frac{W}{h}\right) - 0.385\right] \tag{11}$$

$$k_o = 4.26 - 1.453\ln\left(\frac{W}{h}\right). \tag{12}$$

For $0.1 \leq s/W \leq 0.3$

$$m_e = 0.8675 \tag{13}$$
$$k_e = 2.043(W/h)^{0.12}. \tag{14}$$

For $0.3 \leq s/W \leq 1$

$$m_e = \frac{1.565}{(W/h)^{0.16}} - 1 \tag{15}$$

$$k_e = 1.97 - \frac{0.03}{(W/h)}. \tag{16}$$

The capacitive values calculated for modeling the discontinuity were 0.0192 and 0.0131 pF for C_g and C_p, respectively. From the equivalent π network it is a relatively simple task to convert it into the *ABCD* matrix form. The complete microstrip gap resonator circuit is shown Fig. 9(c).

B. AEC Resonator Equivalent Circuit

The equivalent circuit for the AEC resonator was designed in a very similar way to the microstrip gap resonator. The transmission line sections are modeled by (6) and the equivalent series AEC circuit shown in Fig. 2(c) was used for modeling the capacitive coupling sections. The resulting equivalent circuit is shown in Fig. 10(a). Using this equivalent circuit, the length of the resonating element was estimated to be 6.5 mm to give the same resonant frequency as the previous microstrip gap resonator. A photograph of the resonator is shown in Fig. 10(b).

C. Results

The gap and AEC resonators' equivalent circuit responses were compared against measurement data and CST simulations. Fig. 11(a) and (b) shows transmission coefficient comparisons of the capacitive gap and AEC resonators, respectively, for simulation, equivalent circuit, and measurement data. The plots show that they agree closely. For the gap resonator, the center frequency and insertion loss for the simulation, measured and equivalent circuit data sets varied by 55 MHz and 3.26 dB, respectively. For the AEC resonator the values vary by 98 MHz and 1.3 dB. Fig. 12 shows a comparison of the transmission coefficients between the
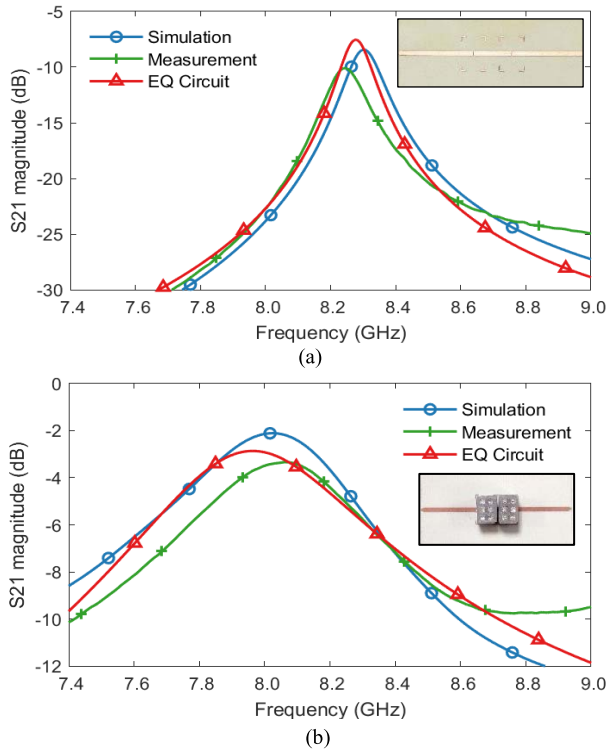
Fig. 11. Simulated, measured, and equivalent circuit resonator S-parameters. (a) Gap resonator comparison. (b) AEC resonator comparison.
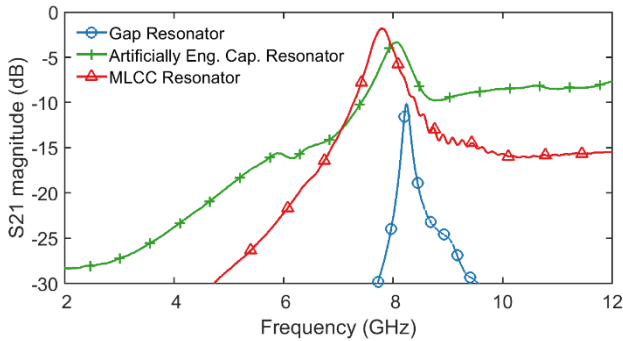

Fig. 12. Measured transmission response of the capacitive gap resonator, AEC resonator, and MLCC resonator.

measured microstrip gap and AEC resonator. For comparison, a resonator containing two 0.1-pF MLCCs as capacitive elements was also measured and the transmission response is also shown in Fig. 12.

The Q factors for the capacitive gap resonator and the AEC resonator was 62 and 13.5 with the insertion losses of 10.1 and 3.3 dB, respectively. Even though the Q factor is lower for the AEC resonator, the insertion loss is less due to better coupling into the resonating element resulting in a lower insertion loss. Material losses in the AEC are the main reason for the lower Q. The Q factor and insertion loss for the MLCC resonator is of similar value to the AEC resonator at 15.5 and 1.8 dB, respectively, showing that both components have comparable losses at 8 GHz

$$\frac{1}{Q_L} = \frac{1}{Q_e} + \frac{1}{Q_0}. \tag{17}$$

By using (17), the Q factor of the AEC and MLCC can be estimated by calculating the external Q factor (Q_e) from the loaded (Q_L) and unloaded (Q_0)Q factor measurements [31]. This number will then be doubled as there are two devices under test. The calculated Q factor of the MLCCs is 41.3 while that of the AEC Q is 34.5. Using the same measurement technique, the two values were found to be quite similar and thus exhibiting comparable losses. If lower loss materials were used like ABS or Teflon and a silver ink, the Q factor could be increased. This is corroborated with simulation results; when the AEC resonator was simulated with an AEC host loss tangent of 0.002 and an inclusion conductivity of 3.33 $\times$ 10^6 S/m, the Q of the resonator increased to 15.2 and the calculated Q of the AEC increased to 40.3.

VI. CONCLUSION

The concept of the AEC as a 3-D printable alternative to conventional capacitors has been demonstrated. The examples in Section III have shown an improvement to effective capacitance value stability over frequency when compared with equivalently valued 0603(IN) MLCCs. The series AEC showed a bandwidth improvement of 26% in the 40% tolerance band, whilst the shunt AEC showed an improvement of 150% and 197 % in the 20% and 40% tolerance bands, respectively. The increase in shunt capacitive stability is particularly impressive as the component's useable capacitive bandwidth has almost tripled. Such improvements are beneficial to applications requiring frequency-stable components, for example, in wideband filters as the change in component value across the frequency spectrum can detune the filter. The AECs measured were 5 times larger than the equivalent MLCC but improved capacitance stability over frequency was still observed. However, as shown in Section IV with improved 3-D printing resolutions, smaller AECs can be manufactured which exhibit capacitance stability over wider frequency ranges.

The AEC's equivalent circuit was also validated by designing an example half wavelength microstrip resonator. The equivalent circuit response was found to be in very good agreement with the simulation and measurement results which validates the circuit model. The resonator example demonstrated that the measured Q factor of the AEC is close to that of an MLCC. With further optimizations to the materials used, losses could be further reduced. Furthermore, Section IV showed with simulation results that with increased 3-D printer resolution and higher permittivity materials, higher capacitance values and wider band performance can be achieved.

The major advantage of manufacturing AECs over conventional components is that they are highly configurable, customizable, and 3-D printable; 3-D printing allows the designer to make variations in the design quickly and without a cost penalty associated with existing tooling. For example, the size and spacing of the inclusions can be changed and alternative dielectrics used to obtain different nominal capacitances and different component characteristic over frequency, as shown in Section IV. Due to the nature of 3-D printing these components can be made on demand which can reduce time spent on prototyping and minimize storage space reserved for storing components of this type. Anisotropic inclusions

are another possibility to obtain different characteristics from different polarizations of the component. 3-D printing also allows for the design of passive monolithic 3-D circuits where the tracks and components can be fabricated into the same package. With the customizable design, it also allows for the electrical characteristics to be tailored to the needs of the application. As AECs utilize thermoplastics standard desktop 3-D printers can be used; unlike with MLCC manufacture which require a multistage manufacturing process that includes high temperature sintering. The major challenges with AECs are the low printing resolution and the availability of high permittivity, low loss 3-D printable materials. Although over time as 3-D printer resolutions increase, dimensions can be reduced further resulting in a more frequency-stable capacitor with a smaller electrical length and lower parasitic elements.

APPENDIX

A. Derivation of Equation to Find Series Lumped Impedance from S-Parameters

This section uses the telegrapher's equations [31] to derive (3) in Section II which is used to extract the series impedance of a component in a typical measurement system. Fig. 13 shows the two-port measurement system with a source and load impedances matched to the impedance of the transmission line and an unknown series impedance.

The following equations are the telegraphers in phasor form and describe the total voltage and current incident on an n-port system in terms of incoming and reflected waves [31]:

$$V_n = V_n^+ + V_n^- \tag{18}$$

$$I_n = I_n^+ - I_n^-. \tag{19}$$

The telegrapher's equations can be used to characterize the characteristic impedance of a line [31]

$$Z_n = \frac{V_n^+}{I_n^+} = \frac{V_n^-}{I_n^-}. \tag{20}$$

As the system in Fig. 13 has a matched source and load, no reflections occur from port 2 and the source impedance absorbs all reflected waves from the unknown impedance Z_{DUT}, thus

$$V_2^+ = 0 \tag{21}$$

$$I_2^+ = 0. \tag{22}$$

The impedance of the series component can be calculated by (23) with V_{DUT} describing the voltage across the component and I_{DUT} describing the current flowing through the component

$$Z_{DUT} = \frac{V_{DUT}}{I_{DUT}} = \frac{V_1 - V_2}{I_1}. \tag{23}$$

This expression can be rewritten using (18) and (21) to remove V_2^+

$$Z_{DUT} = \frac{V_1 - V_2^-}{I_1}. \tag{24}$$

Furthermore, as all current in the system is conserved, the total current from port 1 must equal the current from port 2
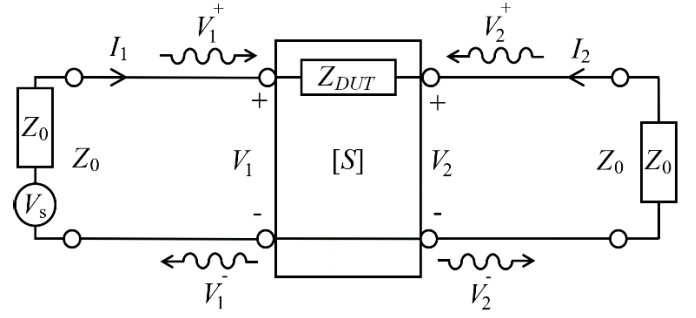

Fig. 13. Signal flow graph of a two-port system with a matched source at port 1, a matched load at port 2, and an unknown series impedance Z_{DUT}.

but in the opposite direction ($I_1 = -I_2$). Thus taking (19) and (22) this can be expressed

$$I_1 = I_1^+ - I_1^- = I_2^-. \tag{25}$$

Using this expression, (24) can be rewritten as

$$Z_{DUT} = \frac{V_1 - V_2^-}{I_2^-}. \tag{26}$$

By applying (20)–(26), we obtain

$$Z_{DUT} = \frac{V_1 - I_2^- Z_0}{I_2^-}. \tag{27}$$

Next, (25) can be applied to have the numerator defined in terms of port 1

$$Z_{DUT} = \frac{(V_1^+ + V_1^-) - (I_1^+ - I_1^-)Z_0}{I_2^-}. \tag{28}$$

Equation (20) is now used to simplify the expression

$$Z_{DUT} = \frac{(V_1^+ + V_1^-) - (V_1^+ - V_1^-)}{I_2^-} = \frac{2V_1^-}{I_2^-}. \tag{29}$$

Equation (20) is used again to define the unknown impedance in terms of voltage phasors

$$Z_{DUT} = 2Z_0 \frac{V_1^-}{V_2^-}. \tag{30}$$

Assuming there are no reflections from port 2, the scattering parameter terms S_{11} and S_{21} are defined by the expressions [31]

$$S_{11} = \frac{V_1^-}{V_1^+} \tag{31}$$

$$S_{21} = \frac{V_2^-}{V_1^+}. \tag{32}$$

Apply both (31) and (32) to obtain the expression defining series Z_{DUT} in terms of its scattering parameters:
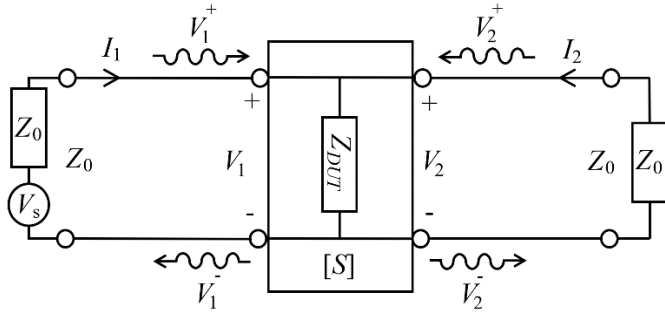
$$Z_{DUT} = 2Z_0 \frac{S_{11}}{S_{21}}. \tag{33}$$

Fig. 14. Signal flow graph of a two-port system with a matched source at port 1, a matched load at port 2, and an unknown shunt impedance Z_{DUT}.

B. Derivation of Equation to Find Shunt Lumped Impedance from S-Parameters

This section uses the telegrapher's equations to derive (4), which is used to extract the shunt impedance of a component from a set of two-port scattering parameters. Fig. 14 shows the two-port measurement system with a source and load impedances matched to the impedance of the transmission line and an unknown shunt impedance.

In shunt impedance case, the voltages V_1 and V_2 are the same while the current through Z_{DUT} is the sum of current from ports 1 and 2

$$V_{\text{DUT}} = V_1 = V_2 \tag{34}$$

$$I_{\text{DUT}} = I_1 + I_2. \tag{35}$$

This leads to expressing the impedance Z_{DUT}

$$Z_{\text{DUT}} = \frac{V_{\text{DUT}}}{I_{\text{DUT}}} = \frac{V_2}{I_1 + I_2}. \tag{36}$$

As there is no reflection from the port 2 load, (36) can be rewritten

$$Z_{\text{DUT}} = \frac{V_2^-}{(I_1^+ - I_1^-) + (0 - I_2^-)}. \tag{37}$$

Equation (20) can be applied to define Z_{DUT} in terms of voltage phasors only

$$Z_{\text{DUT}} = \frac{V_2^-}{1/Z_0(V_1^+ - V_1^-) + 1/Z_0(0 - V_2^-)}. \tag{38}$$

As there is no reflection from the port 2 load (34) can be rewritten as

$$V_1 = V_1^+ + V_1^- = V_2^-. \tag{39}$$

This can then be applied to (37) to have the denominator in terms of voltage from port 1

$$Z_{\text{DUT}} = Z_0 \frac{V_2^-}{(V_1^+ - V_1^-) - (V_1^+ + V_1^-)}. \tag{40}$$

Reducing this equation gives the expression

$$Z_{\text{DUT}} = Z_0 \frac{V_2^-}{-2V_1^-}. \tag{41}$$

Expressions (31) and (32) are finally applied to give the overall expression defining shunt Z_{DUT} in terms of its scattering parameters

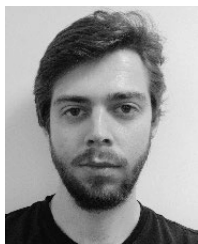$$Z_{\text{DUT}} = -0.5 Z_0 \frac{S_{21}}{S_{11}}. \tag{42}$$

REFERENCES

[1] T. Campbell, A. P. Hibbins, J. R. Sambles, and I. R. Hooper, "Broadband and low loss high refractive index metamaterials in the microwave regime," *Appl. Phys. Lett.*, vol. 102, no. 9, Mar. 2013, Art. no. 091108.

[2] A. K. Amert, B. B. Glover, and K. W. Whites, "A large index of refraction artificial material composed of dumbbell particles," in *Proc. IEEE Antennas Propag. Soc. Int. Symp.*, Jul. 2010, pp. 1–4.

[3] S. Zhang, W. Whittow, and J. Y. C. Vardaxoglou, "Additively manufactured artificial materials with metallic meta-atoms," *IET Microw., Antennas Propag.*, vol. 11, no. 14, pp. 1955–1961, Nov. 2017.

[4] E. A. Parker and B. Sanz-Izquierdo, "3D printing technique for fabrication of frequency selective structures for built environment," *Electron. Lett.*, vol. 49, no. 18, pp. 1117–1118, 2013.

[5] E. A. Parker and B. Sanz-Izquierdo, "Frequency selective surfaces formed by partially metalising 3D printed shapes," in *Proc. 9th Eur. Conf. Antennas Propag.*, 2015, pp. 1–4.

[6] D. S. Lockyer, J. C. Vardaxoglou, and R. A. Simpkin, "Complementary frequency selective surfaces," *IEE Proc.—Microw., Antennas Propag.*, vol. 147, no. 6, pp. 501–507, Dec. 2000.

[7] F. Costa, A. Monorchio, and G. Manara, "Analysis and design of ultra thin electromagnetic absorbers comprising resistively loaded high impedance surfaces," *IEEE Trans. Antennas Propag.*, vol. 58, no. 5, pp. 1551–1558, May 2010.

[8] N. Riauka, A. Chauraya, and J. C. Vardaxoglou, "Compact antenna integrated into flat plate FSS," in *Proc. AP-S IEEE Antennas Propag. Soc. Int. Symp.*, Jul. 2008, pp. 1–4.

[9] G.-L. Huang, S.-G. Zhou, C.-Y.-D. Sim, T.-H. Chio, and T. Yuan, "Lightweight perforated waveguide structure realized by 3-D printing for RF applications," *IEEE Trans. Antennas Propag.*, vol. 65, no. 8, pp. 3897–3904, Aug. 2017.

[10] D. Shamvedi, C. Danilenkoff, S. Karam, P. O'Leary, and R. Raghavendra, "3D printed periodic structures in a horn antenna for side-lobe reduction using direct metal laser sintering," in *Proc. Loughborough Antennas Propag. Conf. (LAPC)*, 2017, pp. 1–4.

[11] E. MacDonald *et al.*, "3D printing for the rapid prototyping of structural electronics," *IEEE Access*, vol. 2, pp. 234–242, Dec. 2014.

[12] E. De Nava *et al.*, "Three-dimensional off-axis component placement and routing for electronics integration using solid freeform fabrication," in *Proc. 19th Annu. Solid Freeform Fabrication Symp.*, 2008, pp. 362–369.

[13] S. W. Kwok *et al.*, "Electrically conductive filament for 3D-printed circuits and sensors," *Appl. Mater.*, vol. 9, pp. 167–175, Dec. 2017.

[14] P. F. Flowers, C. Reyes, S. Ye, M. J. Kim, and B. J. Wiley, "3D printing electronic components and circuits with conductive thermoplastic filament," *Additive Manuf.*, vol. 18, pp. 156–163, Dec. 2017.

[15] T. J. Wasley, "Digitally driven microfabrication of 3D multilayer embedded electronic systems," Ph.D. dissertation, Wolfson School Mech., Elect. Manuf. Eng., Loughborough Univ., Loughborough, U.K., 2016.

[16] T. P. Ketterl, "A 2.45 GHz phased array antenna unit cell fabricated using 3-D multi-layer direct digital manufacturing," *IEEE Trans. Microw. Theory Techn.*, vol. 63, no. 12, pp. 4382–4394, Dec. 2015.

[17] M. Liang, X. Yu, C. Shemelya, E. Macdonald, and H. Xin, "3D printed multilayer microstrip line structure with vertical transition toward integrated systems," in *IEEE MTT-S Int. Microw. Symp. Dig.*, 2015, pp. 5–8.

[18] J. A. Byford, M. I. M. Ghazali, S. Karuppuswami, B. L. Wright, and P. Chahal, "Demonstration of RF and microwave passive circuits through 3-D printing and selective metalization," *IEEE Trans. Compon., Packag., Manuf. Technol.*, vol. 7, no. 3, pp. 463–471, Mar. 2017.

[19] C. Mariotti, M. M. Tentzeris, and L. Roselli, "Demonstration and charaterization of fully 3D-printed RF structures," in *Proc. IEEE 15th Medit. Microw. Symp. (MMS)*, Nov./Dec. 2015, pp. 1–4.

[20] S.-Y. Wu, C. Yang, W. Hsu, and L. Lin, "3D-printed microelectronics for integrated circuitry and passive wireless sensors," *Microsyst. Nanoeng.*, vol. 1, no. 1, pp. 1–9, Dec. 2015.

[21] J. Machac, "Microstrip line on an artificial dielectric substrate," *IEEE Microw. Wireless Compon. Lett.*, vol. 16, no. 7, pp. 416–418, Jul. 2006.

[22] M. Coulombe, H. V. Nguyen, and C. Caloz, "Substrate integrated artificial dielectric (SIAD) structure for miniaturized microstrip circuits," *IEEE Antennas Wireless Propag. Lett.*, vol. 6, pp. 575–579, 2007.

[23] C. C. Njoku, W. G. Whittow, and J. C. Vardaxoglou, "Simulation methodology for synthesis of antenna substrates with microscale inclusions," *IEEE Trans. Antennas Propag.*, vol. 60, no. 5, pp. 2194–2202, Mar. 2012.

[24] I. Bahl, *Lumped Elements for RF and Microwave Circuits*. Norwood, MA, USA: Artech House, 2003.

[25] A. M. Nicolson and G. F. Ross, "Measurement of the intrinsic properties of materials by time-domain techniques," *IEEE Trans. Instrum. Meas.*, vol. IM-19, no. 4, pp. 377–382, Nov. 1970.

[26] W. B. Weir, "Automatic measurement of complex dielectric constant and permeability at microwave frequencies," *Proc. IEEE*, vol. 62, no. 1, pp. 33–36, Jan. 1974.

[27] MG Chemicals. *Silver Conductive Epoxy Adhesive Slow Cure/Extreme Conductivity 8330S Technical Data Sheet*. Accessed: May 8, 2019. [Online]. Available: https://www.mgchemicals.com/products/adhesives/electricallyconductive-adhesives/two-part-epoxy/silver-conductive-epoxy-8331

[28] Xometry. *Design Guide: Fused Deposition Modeling (FDM)*. Accessed: May 8, 2019. [Online]. Available: https://cdn2.hubspot.net/hubfs/340051/Design_Guides/Xometry_DesignGuide_FDM.pdf

[29] Ultimaker. *Designing for Printability*. Accessed: May 8, 2019. [Online]. Available: https://ultimaker.com/en/resources/22015-designing-for-printability

[30] M. Barbuto, A. Alù, F. Bilotti, A. Toscano, and L. Vegni, "Characteristic impedance of a microstrip line with a dielectric overlay," *COMPEL-Int. J. Comput. Math. Elect. Electron. Eng.*, vol. 32, no. 6, pp. 1855–1867, 2013.

[31] D. M. Pozar, *Microwave Engineering*, 4th ed. Hoboken, NJ, USA: Wiley, 2012.

[32] AVX. *RF Ceramic Capacitors—MLOTM Series*. Accessed: May 13, 2019. [Online]. Available: http://www.avx.com/products/ceramic-capacitors/surface-mount/mlo-series-size-0603/

[33] Farnell. *Electronic Component Distributors*. Accessed: May 8, 2019. [Online]. Available: https://www.farnell.com/

[34] RS. *RS PRO 2.85 mm Black PLA 3D Printer Filament, 1kg*. Accessed: May 13, 2019. [Online]. Available: https://uk.rs-online.com/web/p/3d-printing-materials/8320264/

[35] RS. *MG Chemicals Silver Conductive Adhesive Epoxy, 21g Syringe*. Accessed: May 13, 2019. [Online]. Available: https://uk.rs-online.com/web/p/conductive-adhesives/9185009/

[36] A. Zocca, P. Colombo, C. M. Gomes, and J. Günster, "Additive manufacturing of ceramics: Issues, potentialities, and opportunities," *J. Amer. Ceram. Soc.*, vol. 98, no. 7, pp. 1983–2001, Jul. 2015.

[37] D. Wang *et al.*, "Cold-sintered temperature stable $Na_{0.5}Bi_{0.5}MoO_4–Li_2MoO_4$ microwave composite ceramics," *ACS Sustain. Chem. Eng.*, vol. 6, no. 2, pp. 2438–2444, Feb. 2018.

[38] B. Zhang, B. Seong, V. Nguyen, and D. Byun, "3D printing of high-resolution PLA-based structures by hybrid electrohydrodynamic and fused deposition modeling techniques," *J. Micromech. Microeng.*, vol. 26, no. 2, Feb. 2016, Art. no. 025015.

[39] Premix. *PREPERM Stock Shapes*. Accessed: May 21, 2019. [Online]. Available: https://www.preperm.com/products/stock-shapes/

[40] K. C. Gupta, R. Garg, I. Bahl, and P. Bhartis, *Microstrip Lines and Slotlines*, 2nd ed. Boston, MA, USA: Artech House, 1996.

William G. Whittow (SM'12) received the B.Sc. degree in physics and the Ph.D. degree in computational electromagnetics from the University of Sheffield, Sheffield, U.K., in 2000 and 2004, respectively.

From 2004 to 2012, he was a Research Associate with Loughborough University, Loughborough, U.K., where he became a Lecturer of electronic materials integration in 2012. He became a Senior Lecturer in 2014 and a Reader (Associate Professor) of radiofrequency materials in 2018 with the Wolfson School of Mechanical, Electrical, and Manufacturing Engineering, Loughborough University. He has authored more than 215 peer-reviewed journal articles and conference papers in topics related to electromagnetic materials, synthetic dielectrics, dielectric measurements, 3-D printing, wearable antennas, VHF antennas, specific absorption rate, FDTD, specific absorption rate, metamaterials, heterogeneous substrates, embroidered antennas, inkjet printing, electromagnetic compatibility, RFID tags, phantoms, and genetic algorithms.

Dr. Whittow was the Coordinating Chair of the Loughborough Antennas and Propagation Conference (LAPC) from 2007 to 2011. In 2017, he won the Women in Engineering Men As Allies Award. He is an Associate Editor of the *Electronics Letters* and *IET Microwaves, Antennas and Propagation*. He serves on the technical program committees for several IEEE international conferences. He has been asked to give 15 invited conference presentations; a four-day invited workshop on bioelectromagnetics and teach about dielectric measurements at the European School of Antennas. His academic journal articles can be freely downloaded here: http://publications.lboro.ac.uk/publications/all/collated/elwgw.html.

J. (Yiannis) C. Vardaxoglou (F'12) received the B.Sc. degree in mathematical physics and the Ph.D. degree in electronics from the University of Kent, Kent, U.K., in 1982 and 1985, respectively.

He joined Loughborough University, Loughborough, U.K., as a Lecturer in 1988 and was promoted to Senior Lecturer in 1992 and Professor of wireless communications in 1998. He served as the Dean of the School of Electronic, Electrical, and Systems Engineering with Loughborough University from 2011 to 2012. He established the 30-year-old Wireless Communications Research (WiCR) Group, Loughborough University, and founded the Centre for Mobile Communications Research (CMCR). He is the Director of the SYMETA Research Centre (www.symeta.co.uk), Sint-Pieters-Leeuw, Belgium, funded by an EPSRC Grand Challenge award, researching in wide-ranging topics applicable to cutting-edge wireless communications technology. He has authored over 400 refereed journals and conference proceeding articles (with over 7500 citations) and has written a book on FSS. He holds six patents. His current research focuses primarily on metamaterial structures, additive manufacturing (3-D printing) for RF/micro-/millimeter-wave engineering.

Dr. Vardaxoglou was elected a Fellow of the Royal Academy of Engineers in 2011 and the Institute of Electrical and Electronics Engineers in 2012. He was recently awarded a prestigious EPSRC's Grand Challenge £5M (FEC) Award: Synthesizing 3D Metamaterials for RF, Microwave and THz Applications, (http://gow.epsrc.ac.uk/NGBOViewGrant.aspx?GrantRef=EP/N010493/1). He has served as a Consultant to various industries and is the Technical Director of Antrum Ltd. He has attracted research funding from industry and has been awarded 18 EPSRC research grants. He was the Chairman of the Executive Committee of IET's Antennas and Propagation Professional Network in the U.K. and the Chair of the IEEE's distinguish lecturer program of the Antennas and Propagation Society (APS) for five years. He founded the Loughborough Antennas and Propagation Conference (LAPC), which has been running since 2005. He has chaired numerous IEE//IET events and has served on the Steering Committee of the European Conference on Antennas and Propagation, EuCAP. He was the General Chair of EuCAP '07.

Tom W. Whittaker received the M.Eng. degree (first class) in electronic and electrical engineering from Loughborough University, Loughborough, U.K., in 2016. He is currently pursuing the Ph.D. degree.

He joined the SYMETA Research Centre (www.symeta.co.uk), Sint-Pieters-Leeuw, Belgium in 2016. His current research interests include equivalent circuit modeling of metamaterials and the design and manufacture of 3-D printed metamaterial components for RF and microwave applications.